Communications Earth & Environment

Article in Press

https://doi.org/10.1038/s43247-026-03203-w

# The growing threat of spatially synchronized dry-hot events to global ecosystem productivity

Received: 20 June 2025

Accepted: 8 January 2026

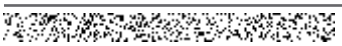

Cite this article as: Hassan, W.u., Nayak, M.A., Saharwardi, M.S. *et al.* The growing threat of spatially synchronized dry-hot events to global ecosystem productivity. *Commun Earth Environ* (2026). https://doi.org/10.1038/s43247-026-03203-w

**Waqar ul Hassan, Munir Ahmad Nayak, Md Saquib Saharwardi, Harikishan Gandham, Hari Prasad Dasari, Caspar Ammann, David Yates, Ibrahim Hoteit & Yasser Abualnaja**

# The growing threat of spatially synchronized dry–hot events to global ecosystem productivity

Waqar ul Hassan[1,2], Munir Ahmad Nayak[3], Md Saquib Saharwardi[1,2], Harikishan Gandham[1,2], Hari Prasad Dasari[1,2], Caspar Ammann[4], David Yates[4,] Ibrahim Hoteit[1], and Yasser Abualnaja[1,2]

[1] Physical Sciences and Engineering, King Abdullah University of Science and Technology, Thuwal, Saudi Arabia

[2] Climate Change Center, King Abdullah University of Science and Technology/National Center for Meteorology, Jeddah, Saudi Arabia

[3] Department of Civil Engineering, National Institute of Technology, Srinagar, Jammu and Kashmir, India

[4] National Center for Atmospheric Research, University of Massachusetts Amherst, Boulder, Colorado, USA

Correspondence to: Yasser Abualnaja (yasser.abualnaja@kaust.edu.sa)

## 1 Abstract

Compound hazards, like simultaneous occurrence of unusually dry and hot (DH) weather, cause cascading socio-economic damages that surpass univariate hazards. In the context of agricultural production, DH events triggered by pressure and moisture flux anomalies are responsible for some of the most severe agricultural losses across the globe. Most analyses focus on characterizing compound events in individual regions, and the extent of spatial synchrony of DH events and their impacts on crop production has yet to be quantified. Here, using observation-based gridded precipitation and temperature data, we find that the frequency of widespread spatial synchrony–defined as five or more regions simultaneously experiencing DH events–has increased nearly ten-fold over the past four decades, while confined events are declining. This rapid synchronization, especially in recent decades, reflects a non-linear response to global warming. At global scale, substantially larger productivity losses are observed during widespread DH events as compared to the spatially confined DH events. Wheat cropland exhibits the strongest losses during synchronized DH events, followed by maize, with weaker effects for rice. The results highlight the importance of considering the growing occurrence of spatially widespread DH events in assessments of agricultural risk, alongside analyses of individual regional extremes.

## 2 Significance:

Our study presents the first global-scale evidence that compound DH events–where extreme heat and drought co-occur–have become significantly more synchronized and widespread since 2000. This shift appears to be driven by accelerated global warming. Unlike earlier studies limited by seasonal or regional analyses, our fine-scale, sub-seasonal approach reveals that synchronized DH events are now affecting multiple key breadbasket regions simultaneously, amplifying crop losses and threatening global food security. These findings highlight a critical tipping point in the climate

system and call for urgent action to strengthen early warning systems, climate-resilient agriculture, and international coordination to mitigate the growing risks of simultaneous climate extremes.

Key words:

Compound dry and hot events, Primary productivity, Crop yield, Global warming, Spatial synchronization

## 3 Introduction

Over the past two decades, several episodes of catastrophic losses in the production of staple crops such as wheat, rice, and maize, have been attributed to dry and hot weather conditions occurring simultaneously over a region [1–5]. The co-occurrence of multiple hazards over a region is defined as a compound hazard event [6]. They are often associated with impacts that are more severe than from a univariate event. Compound dryness and heat stress impose cascading limitations on crop growth due to their nonlinear dependence [7,8]. To maintain water, plants partially or fully close their stomata during drought or heatwaves, which decreases their $CO_2$ intake, yet it increases its release through respiration. At excessive temperatures, however, stomata remain open to allow for sufficient transpiration to regulate heat and thus limiting damage [8,9]. Both water stress and heat stress also directly damage plant tissue. The net outcome is an imbalance in the carbon cycle, poor nutrient assimilation, and inefficient photosynthesis [10,11]. During DH events, the impact on plant growth depends not only on the availability of water and the magnitude of heat stress, but several other factors can play important roles, including crop physiology, climatic zone, and availability of irrigation water [7,12]. Thus, multiple possible growth-inhibiting pathways exist during DH events, and disentangling the individual contributions on yield is complex [13]. Several studies have attempted to quantify the net effect on crop yield during DH events. For example, the 2018 summer DH events in Europe resulted in up to 40% harvest losses for multiple crops in northern and eastern Europe [4], which led to a steep rise in the prices of wheat and barley [14]. In India, DH events have been responsible for the six largest staple food crises during the past six decades [15].

Univariate analyses of heatwaves or droughts tend to underestimate their associated risks, for they often co-occur as DH events. During boreal summer of transition climate zones (land regions that are neither too dry nor too humid), such as parts of the central United States, parts of Europe, South

Asia, and Russia, among others [16], low precipitation and soil moisture can co-occur with high temperatures [17,18]. The positive feedback through land-atmosphere coupling is believed to enhance the prevalence of DH events in these mid-latitude regions [19]. Superposed on this variability, the recent widespread warming linked to climate change has increasingly played a multifaceted role in changing the occurrence and intensity of DH events and has likely enhanced the land-atmosphere coupling [20–22].

Several recent studies have reported a rise in DH events globally and regionally, with mid-latitude regions often appearing as hotspots for such events and are expected to increase, in some regions a doubling [16,19,23–25]. A spatial and temporal connectedness in weather extremes among several regions across the globe have recently been attributed to specific long-wave circulation patterns and climate modes[26–29]. Mid-latitude Rossby waves, for example, offer a known mechanism to establish circum-global, stationary wave patterns that can trigger dry or hot events in multiple regions simultaneously [28,30–32]. Similarly, the tropical El-Niño Southern Oscillation, the dominant mode of internal climate variability, is often found to cause synchronized dry or/and hot events in the tropical land mass [26–28] via the atmospheric bridges [33]. While identifying systematic changes in the frequency and intensity of these dynamical modes of variability remains elusive, the increase in background warming of the climate is likely enhancing the frequency and occurrences of heatwaves everywhere on the land [19,24,31,34,35]. A recent study on the spatial extent of compound heatwaves attribute the eight fold increase in synchronized heatwaves post-2000 to anthropogenic warming [26]. The systematic increase of likelihood of these heatwaves due to warming will inescapably coincide more frequently with future droughts, resulting in DHs [34]. Linking this research on atmospheric teleconnection of dry and/or hot events, we propose that accelerated background warming along with increasingly accentuated atmospheric anomalies due to

anthropogenic climate change[36,37], leads to DH events that will increasingly occur simultaneously in multiple regions. We call this *spatial synchrony in DH events*.

While regional extreme events can disrupt local agricultural production, their impacts are often partially moderated through trade and redistribution. For instance, multi-year droughts cause prolonged and severe food security challenges, but losses in one region can be offset by trade from other unaffected regions. In contrast, when such extreme events occur simultaneously across multiple major crop-producing regions, particularly the key breadbaskets, the scope of affected areas increases and can place greater strain on international markets, even over relatively short time scales. Previous studies show that widespread droughts and heatwaves are associated with reductions in crop production of approximately 4–10% at global and national scales [7,30,38–40], highlighting the potential significance of spatially synchronized hazards. Such synchrony increases the likelihood of concurrent yield reductions in staple crops and may limit the buffering capacity of international trade. In addition to direct production losses, widespread events have been linked to heightened market sensitivity and volatility[41], which can further influence food security. Beyond agriculture, synchronous dry–hot events have also been associated with reductions in terrestrial carbon uptake at global scales[42], affecting an important ecosystem service related to climate regulation. Despite these implications, the extent to which synchronized dry–hot events influence vegetation productivity and crop yields across regions remains incompletely understood. Quantifying these impacts is therefore important for characterizing the aggregate risks posed by widespread dry–hot conditions to both ecosystems and agricultural production, without implying effects beyond those captured by aggregation alone.

To manage these cascading risks, it is necessary to understand the spatial connectedness of DH events. Studying synchrony provides a more realistic assessment of their potential to trigger

widespread, systemic losses than analyses restricted to isolated regional events. Moreover, because DH events are highly sensitive to climate change, documenting observed trends in their spatial synchrony is also critical for evaluating models and improving projections. In this work, we first identify the regions of synchronous DH events and then quantify and attribute their changes in occurrence to large-scale background warming trends in temperature. Finally, illustrate the impact of widespread DH events on ecosystem productivity.

# 4 Results

## 4.1 Robust synchronizations in DH events

To explore the spatial synchrony in DH events (defined when a dry week co-occurs with a hot week; see Methods for details), we use the 44 reference regions (excluding Antarctica) defined in IPCC AR6 region (see Table S1 for definitions). A regional DH event/week (RCDH) is then defined when at least 5% of the region's area is under a DH event (details in Methods). Using the Likelihood Multiplication Factor (LMF) [19] to measure the strength of spatial synchrony, several neighboring regions appear to have statistically significant spatial synchrony (Figure 1). Spatial synchronization within the adjacent regions, such as Central North America and Eastern North America, is perhaps not surprising given their proximity and absence of physical boundaries. Sometimes droughts and heatwaves, thus DH events, also extend to neighboring regions through self-intensification and self-propagation [43,44].

Interestingly, LMF also shows that synchrony is not limited to immediate neighbor regions. Figure 1a indicates examples of robust teleconnections across the globe (more than 10,000 km). For example, the spatial synchrony between South America and Central Africa, South America and

South Africa and Australia, Canadian regions and East Asia, and Europe and South Asia. Long-distance teleconnections are well-known in the tropics due to, for example, the far-reaching effects of El-Niño as reported by Hassan and Nayak [27], Hassan et al [26], and Singh et al [28]. The strength of their concordance suggests that the spatial synchrony in these regions with regard to DH events is significantly larger than expected under the assumption of independence of weather, i.e., there is no physical/atmospheric connection between the regions (Figure 1). In certain cases, the observed probability of synchrony in two regions is more than double (LMF > 2) than what would be expected under independence. The statistical significance of the results is estimated using binomial tests and a bootstrapping approach (Figure S1).

## 4.2 Rise in spatial synchronization of DH events

After identifying robust pairwise links, the changes in wider spatial synchrony in DH events are explored. Figure 2 indicates a strong rising trend in the spatial extent (0.75% per decade) as well as in the number of regions (0.86 regions per decade) experiencing synchronous DH events. The signal appears to be largely related to rising occurrences of hot events/heatwaves (~4.0% in area and four regions per decade) in the last four decades (Figure 2a, b). In contrast, the areal extent and number of regions with synchronized dry events/droughts appear to have remained relatively unchanged. The mean of the post-2000 distributions of the areal extent and the number of IPCC regions affected by DH event, has almost doubled, which is solely attributed to the intensification of the heatwaves (Figures 2c, d and S2). Equally, the substantial year-to-year variability in spatial synchrony in DH events is largely driven by hot events. DH events with only limited regional links (hereafter confined DH events; 1 or 2 IPCC regions experiencing synchronous DH events) show a clear decline from nearly 27 weeks in the 1980s to 10 weeks in recent decades (Figure 2e). In contrast, a substantial increase, nearly ten-fold jump (from 2 weeks in 1980's to 24 weeks in recent

decade) since the 1980s, is observed in widespread DH events (5 or more IPCC regions experiencing synchronous DH events). This dramatic rise in spatial synchrony in DH events arises from the consistent upward trend of temperature, increasing the likelihood of heatwaves, while the areal extent in droughts appears nearly stationary.

### 4.3 Role of global warming

The changing characteristics of heatwaves have been mainly attributed to climate change [11,26,31]. Here, we assess how widespread warming has influenced the extent of synchrony in DH events, using actual (actual temperature data) and detrended (detrended temperature data) data scenario (for details, see Methods). Figures 3a-b illustrate the spatial extent and the number of regions with synchronous DH events in actual and detrended scenario. Minimal differences are found in DH characteristics between the two analyses during the pre-2000 period, suggesting a limited effect of global warming on synchrony in that period. However, in the post-2000 period, DH events in the actual scenario show a significantly larger mean and spread–about double–compared to the detrended scenario as well as against the pre-2000 period. The significant warming over the past two decades appears to have a substantial effect on the spatial synchrony of these events (Figures 3c, d). Most notably, the mean shift in the post-2000 actual scenario distribution is about 6–7 times that of the detrended scenario distribution, attributing roughly 80–85% of the increase in synchrony to global warming (estimated as difference of means of post-2000 in actual and detrended scenario) and 15–20% to climate variability and indirect warming effects (difference of means of post-2000 and pre-2000 periods of detrended scenario). Due to global warming, the risk of widespread DH events has increased by ~23% in the actual scenario compared to the detrended scenario (~6%), underscoring an accelerated, non-linear response of DH events to global warming. In contrast, the post-2000 risk of spatially confined DH events has seen a reduction to 23.4% in

the actual scenario compared to 46.7% in the detrended scenario. The global rise in temperature is thus responsible for more broadly synchronizing DH events while in a non-warming world, the individual anomalies appear more random and thus less coordinated.

### 4.4 Larger productivity losses during synchronous DH events

DHs have been associated with substantial reductions in crop yields and ecosystem productivity[7,45]. The identified increase in spatial synchrony in these events highlights the growing risk to food productivity at both global and regional levels. We proceed to quantify the effects of dry events, hot events, and DH events on local gross primary productivity (GPP) and crop yield (Figures 4 and 5). While all three event types tend to decrease primary productivity across global land and cropland areas, dry events generally cause more significant reductions than hot events, and the combined impact in DH events further amplifies these losses (Figures 4, and S3-5). Notably, primary productivity losses in croplands are ~1.5 times higher than in global land areas during DH events (Figure 4a). Although above-normal productivity is occasionally observed during univariate hot or dry events, DH events result in almost inevitable losses, particularly in the lower tail (Figures 4a and S4). This tail-heavy behavior underscores a nonlinear response, where the joint occurrence of heat and dryness dramatically increases the likelihood of extreme GPP losses. Rather than acting independently, these stressors interact synergistically, intensifying vegetation stress well beyond the sum of their individual effects. At global scale, substantially larger (double) productivity losses are observed during widespread DH events as compared to the spatially confined DH events (Figures 4b and S6). The average global GPP loss during a widespread DH event (week) is about 0.75% of the global GPP, corresponding to ~2.0 Mt C $d^{-1}$. These results are corroborated by the statistically significant negative relationships between change in GPP (detrended and actual) and both percentage area and number of IPCC regions

simultaneously under DH events (for detrended and actual) (Figures 4c and S7). These relationships primarily capture the scaling of aggregate productivity losses with increasing spatial extent and coherence of DH exposure, rather than isolating distinct local-scale response mechanisms. Accordingly, widespread DH events, by affecting larger areas simultaneously, are associated with greater total productivity losses than spatially confined events (Figures S6 and S8).

At the crop scale, wheat croplands exhibit larger weekly productivity losses than rice and maize for comparable increases in synchronous DH extent (Figures 4c and S7). For wheat, losses amount to approximately 0.17% of GPP per 1% increase in affected area and 0.3% of GPP per additional affected region, compared to ~0.07–0.09% for rice and maize. This higher sensitivity in wheat can be attributed to a significant rise in the persistence of DH events in the wheat growing regions [46], particularly in Eastern Europe, where longer-lasting and recurrent hot-dry conditions extend across the growing season. Because such persistent events are not independent in their impacts, the stress they impose accumulates over time, compounding damage and resulting in disproportionately higher productivity losses per event. Wheat is also more vulnerable to elevated temperatures during critical phenological stages, which further magnifies the impact of persistent DH events [8,46,47]. The maize and rice, on the other hand, are more sensitive to water stress, and hence, the impact is often mitigated by increasing irrigation [7,8]. Previous model-based studies have also reported higher crop loss in wheat than in maize and rice during DH events [45]. Globally, primary productivity declines by about 3.4 Mt C $d^{-1}$ (~ 1.35% of global GPP) for every 10% increase in synchronous DH area and about 0.25 Mt C $d^{-1}$ (~ 0.09% of global GPP) for one additional synchronous DH region (Figure S9 for annual cycle of global GPP). Pantropical forests show comparatively smaller GPP reductions than croplands and grasslands, likely reflecting deeper rooting systems and greater access to subsurface water during DH conditions (Figures S3 and S10). Grasslands experience the

largest losses, consistent with shallow root systems and limited buffering capacity against water stress.

Excluding near-polar regions (south of 40°S and north of 50°N), DH events lead to consistent declines in the crop- and global-land primary production in both hemispheres (Figure 4e). Within this band, the losses appear lowest near the equator, which may be related to the combination of more resilient vegetation, and higher normal primary production (GPP during the normal weather conditions; see methods for details). Larger percentage losses are experienced in the southern subtropics (~22°S to ~35°S) compared to the corresponding northern subtropics for similar bassline GPP, likely linked to more limited irrigation infrastructure and a higher prevalence of rainfed agriculture in these regions [48,49].

Despite the influence of climate extremes on plant health and biomass assimilation, crop yield depends on multiple factors, including technological advances and biological and environmental factors [50]. The intensity and persistence of the climate extremes also play a crucial role in plant recovery and, thus, in loss in crop yield [51,52]. The crop yield is also influenced by the univariate droughts, heatwaves, and other climate extremes, which co-occur alongside with synchronized DHs in the crop growing regions. The impact of these univariate extremes on the yield is not considered in our analysis. Despite that, we find generally negative, though not always statistically significant, relationships between detrended global annual yield and detrended annual frequency of widespread synchronous events/months and spatial extent during the critical growing stages of flowering, pollination, and maturation (Figure 4d). Comparable negative associations are also observed between detrended annual yield and both the annual mean synchronous DH area and the monthly maximum synchronous DH area for the selected crops, across both the critical phase and the full growing season (Figure S11). The robustness of this negative association is further

supported by the consistent decline in crop yields with increasing annual mean synchronization (i.e., the mean number of dominant cropping regions simultaneously affected by DH) and annual maximum synchronization (i.e., the maximum number of regions simultaneously affected) of DH events (Figure S12). To assess the relative roles of spatial extent and frequency of synchronization, we applied a generalized linear model including both total DH-affected area and the number of synchronized events as predictors, along with their interaction. The results indicate negative associations between yield and the frequency of synchronized DH events even after accounting for total affected area (Table S2), though these relationships should be interpreted as reflecting combined scaling and synchronization effects rather than isolated causal mechanisms. Wheat shows the strongest sensitivity, followed by maize, with weaker and less robust associations for rice (Figures 4d, S11, and Table S2).

Although global ecosystem productivity tends to decline during periods of synchronized DH events, the effects are often more evident in regional analyses of key agricultural areas, particularly the breadbasket regions (Figure 5). For instance, during the main wheat growing season (Table S3), productivity in wheat croplands decreases by 2.17–3.94% of regional total productivity for every 10% increase in synchronous DH area in Europe and Australia, respectively, roughly 1.5 and 2.2 times larger than the corresponding global average. Similarly, maize cropland in Europe and South Africa experiences losses nearly twice the global percentage. These stronger regional reductions are associated not only with limited irrigation but also with the higher frequency and persistence of DH events[23,46], which cumulatively reduce cropland productivity. They also suggest a potential super-additive effect of synchronized DH, for instance through impacts on shared water resources. The negative relationship between primary productivity and DH synchronization is supported by statistically significant correlations (5% significance level) exceeding 0.5 (Figure 5,

Table S5). In contrast, wheat and maize croplands in North America, South America, and West Africa exhibit relatively smaller losses than the global average, likely due to more efficient water management, extensive farming practices, and fewer persistent DH events[7,23]. Asian croplands, despite being heavily irrigated, show productivity reductions comparable to global averages, reflecting the influence of frequent DH events and less effective mitigation practices. Interestingly, when considering all land cover types, productivity losses outside Asia and Europe are often larger than those in croplands, mainly because grasslands, which experience substantial GPP loss during DH events, are prominent in these regions, whereas forests dominate in Asia and Europe (Figure S10).

## 5 Conclusions and Discussion

The last two decades have witnessed significantly larger areal extents and annual variability in heatwaves as well as DH events relative to the pre-2000-period (1980–2000). Previous studies have observed increases in the areal extent of heatwaves under global warming [26,31] while detecting only limited changes in drought extents [53]. Increasing heatwaves have been shown to be the primary driving factor for changes in the spatial extent of DH events in the observational period. However, in a warmer world, where moderate heatwaves could become ubiquitous and everywhere, the future synchronization of DH events will primarily depend on the synchrony of droughts. A similar conclusion was reported by Bevacqua et al [34]. Based on the actual and detrended scenario, the post-2000 increases in synchrony in DH extents are likely due to continued global warming. The influence of large-scale warming prior to 2000 had remained somewhat constant. But as if the warming hit a tipping point around 2000 [54,55], synchrony in DH events have been on the rise since then, possibly enhanced by non-linear effects of warming on land-atmosphere feedbacks.

The simple synchronization pairs in DH events identified here are valuable for understanding how extreme weather events are connected across different parts of the globe. However, the teleconnections observed here for the increasingly synchronized DH events appear distinct from the ones found in univariate hot and dry event cases reported in Zhou et al [35], Hassan et al [27], and Singh et al [28]. The reason for such a distinction is that the earlier studies mainly consider mean or cross-summer season (June-July-August) compound events, and often in limited regions (confined DH events). However, such a long-period perspective is affected by loss in signal due to averaging. When refining the temporal scales to the weekly and sub-seasonal timescales, a more comprehensive view of synchronization in DH events becomes possible and a marked increase in occurrence of synchrony in compound events has been revealed for the last two decades.

An important consequence of the synchronous DH events is their increasing impact on crop production. The combination of dry and hot conditions in DH events amplifies productivity loss, an effect further magnified in spatially widespread synchronous DH events rather than confined DH events. In the major maize- and wheat-producing regions, the primary production and yield are highly sensitive to the spatial extent of DH as well as regional synchronization of DH events. The growing extent of DH events results in primary productivity losses across large areas of the globe, excluding higher-latitude regions. The smaller losses in the northern hemisphere polar regions in Figure 4b are likely due to increased water availability due to the melting of snow and glaciers during heatwaves in compound events [56,57]. The higher losses in the southern hemisphere compared to the north, on the other hand, may be due to the lack of proper irrigation as they are primarily rainfed cropping systems.

The reported GPP and crop yield losses associated with spatially synchronized DH events should be interpretted as reflecting a combination of scaling effects and potential super-additive impacts

at the local scale. The scaling effect arises because synchronization increases the number of regions simultaneously experiencing local DH stress, naturally enlarging the aggregate impact. Super-additive impacts may also contribute, potentially through mechanisms such as depletion of shared water resources, reduced availability of irrigation or soil moisture, or increased competition for agricultural inputs, as well as broader system-level amplification due to coherent atmospheric conditions and land–atmosphere interactions during widespread events. Importantly, our analysis does not separate or quantify the relative contributions of these mechanisms. Therefore, while widespread synchronization is associated with larger overall GPP and yield losses, these results should not be interpreted as evidence of purely super-additive effects at individual locations. Rather, they provide an integrated estimate of productivity losses under widespread synchronized DH exposure and highlight the need for future studies to explicitly disentangle the relative contributions of scaling versus amplification pathways and to explore the physical and socio-economic processes that may enhance super-additive effects.

Our results identify the non-linear effects of warming on the extent of DH events, and especially their increased spatial synchronization. Since 2000, the observed rapid increase in synchronized events and their outsized impacts on food security demand critical need for further investigations of the driving mechanisms that guide these weather and climate events. It is recommended to prioritize international collaboration to enhance early warning systems that can track and predict these events across regions. Investments should be directed towards improving regional climate models to better understand these of simultaneous climate extremes and anticipate their global impacts. Additionally, nations should support through establishing an irrigation infrastructure to ensure sufficient water supply during extreme events and promote the development and adoption of climate-resilient crop varieties to maintain agricultural productivity. To further safeguard food

security, international agencies must prioritize the setting up of global food reserves and market stabilization strategies to mitigate economic disruptions caused by widespread crop failures during synchronized events.

# 6 Data and Methods

## 6.1 Data

The present study employs high-resolution daily precipitation and daily maximum temperature from the National Oceanic and Atmospheric Administration (NOAA) Climate Prediction Centre's (CPC) Global Unified Gauge-Based Analysis of Daily Precipitation and Temperature dataset [58]. The data covers the global land at a spatial resolution of $0.5° \times 0.5°$ and is available from 1st January 1979 to the present; however, we used it till 31st Dec 2022 (i.e., 44 years). CPC data are derived from in-situ gauge observations and provide high spatial and temporal accuracy, especially over land and in regions with sparse monitoring networks. This makes CPC a reliable observational baseline for capturing localized extremes compared to the model-based reanalysis products like ERA5 and MERRA-2. Importantly, CPC precipitation is used to bias-correct land-based precipitation in MERRA-2, enhancing its accuracy [59], while ERA5 does not incorporate observational precipitation and often exhibits biases over complex terrain [60]. Also studies have found that CPC data outperforms other gauge based gridded products [61].

The conventional methods of compound drought and heatwave analysis usually estimate the droughts at a monthly timescale [24,35,45,46], which potentially compromises the valuable sub-monthly information of compound event development as the heatwaves evolve over a period of days to week. Therefore, the present study estimates dry and hot events on a weekly time scale to

investigate the DH events by aggregating the daily precipitation and temperature to weekly totals and weekly averages, respectively.

The monthly crop-physical area data for the three selected staple crops (Rice, Maize, and Wheat) was obtained from the "GAEZ+_2015 Monthly Crop Data" dataset [49,62,63], available at a high spatial resolution of 30 arc-minutes. This dataset provides physical area areas for each crop across all 12 months based on crop data from the FAOSTAT database. The crop area for 2015 is computed as the average crop area of three years, i.e., 2014–2016. For each crop, the crop area is also divided into sub-crops to account for crop rotation. The details about the dataset can be found in Grogan et al [49] and references within. For this analysis, which is conducted on a weekly time scale and at a spatial resolution of 0.5°, the monthly crop area data is converted to a weekly scale by assuming the same crop area for each week within a given month and by adding the total of crop area in the big grid (36 grid of 30 arc-min correspond to 1 grid of 0.5° ). The monthly crop area maps are shown in Figures S13-S16.

Daily estimates of global gross primary production (GPP) were obtained from the FluxSat v2.0 dataset, which provides data at a high spatial resolution of 0.05° for the period 2000 to 2019. These estimates are based on observations from MODIS instruments onboard NASA's Terra and Aqua satellites. The dataset leverages the MCD43C4v006 Nadir Bidirectional Reflectance Distribution Function (BRDF)-Adjusted Reflectances (NBAR) product as input for neural networks, specifically trained to upscale GPP using measurements from selected FLUXNET 2015 eddy covariance tower sites. By integrating FLUXNET eddy covariance data with concurrent satellite observations, FluxSat v2.0 ensures a robust estimation approach based on the methodology outlined by Joiner and Yoshida (2020)[64]. Similar to cropland area analysis, we converted GPP to a weekly time scale by averaging over the week and to a spatial resolution of 0.5° by taking the area-

weighted average of smaller grids (100 grids at 0.05° correspond to 1 grid of 0.5°). If the GPP for any week is less than 1 g C $m^{-2}$ $d^{-1}$, we consider that week as a non-vegetative week for the grid cell and, hence removed from analysis. It is important to note that the gridded GPP (g C $m^{-2}$ $d^{-1}$) was multiplied by the grid area to get the total productivity in each grid (in g C $d^{-1}$). For cropland, we used cropland area to get the GPP associated with crops. The annual global yield data for the three selected crops was retrieved from the Food and Agriculture Organization [65] (FAO).

## 6.2 Dry and Hot event definition

Among the multiple drought indices available, we used standardized precipitation index (SPI) [66] at a time scale of 3 weeks to identify the drought weeks/ dry events [drought is used for dry event in Methods]. SPI is selected because it only uses precipitation and does not account for temperature-related water deficiency/dryness like other indices such as standardized precipitation evapotranspiration index (SPEI) [67]. The use of such temperature-dependent drought indices would overestimate the DHs by giving higher weightage to the temperature. At each grid cell, a drought/dry week is defined when the SPI is less than -1. However, the SPI computations in the present study is limited only to the climatologically wet calendar weeks [defined as the calendar week that has non-zero (at least 1 mm) 3-week accumulated precipitation for more than 30% of years [during the study period] and to the grid cells that are not permanently dry [defined as grid cells that have less than 22 wet calendar weeks (~5 months) in a year]. For consistency, we used 1979–2000 as the reference period for both drought (SPI) and heatwave calculations.

Heatwaves are usually defined as the period of anomalously high temperatures that last at least for 3 days. However, the present study uses weekly average of daily maximum temperature ($T$) and hence defines a heatwave week/hot event [heatwave is used for hot events in Methods] when the weekly temperature exceeds the climatological 90th percentile threshold for that week ($T_{90}$). At

each grid cell, the $T_{90}$ threshold is computed for each calendar week using a 3-week window centered on the week during the period 1979-2000 (22 years). This procedure results in spatially- and temporally- varying thresholds to identify heatwave weeks in all seasons, thus ensuring consistency across different seasons and regions. We also set a lower limit of $T_{90}$ threshold as $0°C$ to avoid the identification and inclusion of cold frosty spells as warm spells [68,69]. At each grid cell, if a heatwave week occurs concurrently with a drought week, we define that week as a DH week. The total global land area computed by summing areas of grid cells under droughts, heatwaves, and DH in a week is defined as the global drought, global heatwave, and global DH extents, respectively. The annual extents are then computed by averaging the extents over all the days of the year.

## 6.3 Regional DH event

In order to define the regional extreme weeks, the global land mass (excluding Antarctica) is divided into 44 reference regions as per the Intergovernmental Panel for Climate Change's (IPCC) sixth assessment report (IPCC 2021)[70,71]. For each region, we compute the regional area affected by the drought, heatwave, and DH and call that as regional drought extent, heatwave extent, and DH extent, respectively. A regional drought (heatwave) week is then defined when the drought (heatwave) extent of the region for the week exceeds the 80th percentile of the non-zero [considering only positive extent] regional drought (heatwave) extent for the week and extends over at least 15% of the region's total land area. These thresholds are based on established criteria from previous studies [26–28] and are designed to focus specifically on large-scale events. A regional DH week is then defined when a regional drought week co-occurs with a regional heatwave week, and the regional DH extent is more than 5% of the region's total area [meaning there is a minimum 5% overlap between the drought and heatwave in the region]. At the same time, the DH should

exceed the 80th percentile of non-zero regional DH extent. The 15% lower limit was relaxed to 5% for DH due to the relatively smaller spatial extents of DH and to obtain a reasonable sample size of DH events.

### 6.4 Identifying and attributing synchronization of DH events

If two or more IPCC regions experience regional DH week simultaneously, we call that week the spatially synchronized DH week for these regions. The synchronized DH events are divided into three categories: confined events (affecting one or two regions), medium scale events (affecting three or four regions), and widespread events (affecting five or more regions simultaneously). In this study, risk is quantified as the exceedance probability, representing the likelihood of a specific event, such as widespread DH events/weeks, occurring over a given period. To attribute changes in the spatial synchrony in DHs to global warming, we employ a detrended temperature scenario that isolates the role of temperature trends [72]. Two independent scenarios are developed to assess changes in the risk of synchronization of DH between the pre-2000 and post-2000 periods. The actual scenario uses the observed weekly temperature time series for calculating heatwave and DHs, while the detrended scenario removes the temperature trend by detrending the weekly temperature time series.

Detrending is performed by subtracting the linear regression fit, calculated on a weekly basis for each grid cell, from the observed temperatures. This procedure removes the long-term warming signal and allows us to better isolate interannual variability. While linear detrending cannot capture all aspects of nonlinear change, it provides an efficient and widely used method for removing background warming [73,74] . Importantly, the indirect influence of climate change, through its modification of internal variability, remains present in the detrended series. For each scenario, DH events are computed based on the respective temperature time series, and the risk of spatial

synchronization is calculated. The change in the risk of spatial synchronization between the pre-2000 and post-2000 periods is estimated for both actual and detrended scenarios, and the difference in these changes is attributed to global warming. The change in risk of synchronization between pre- and post-2000 for detrended represents the changes attributed to internal climate variability and indirect effect of global warming. Mathematically, the change attributed to global warming is expressed as:

$$\Delta R_{global\ warming}\ (\%) = 100 \times \left(\left(R^{actual}_{post-2000} - R^{actual}_{pre-2000}\right) - \left(R^{detrended}_{post-2000} - R^{detrended}_{pre-2000}\right)\right) \quad [1]$$

$$\Delta R_{climate\ variability}\ (\%) = 100 \times \left(R^{detrended}_{post-2000} - R^{detrended}_{pre-2000}\right) \quad [2]$$

Where $\Delta R_{global\ warming}\ (\%), and\ \Delta R_{climate\ variability}\ (\%)$ represents the percentage change in the risk of spatial synchronization attributed to global warming and climate variability. This approach enables us to isolate the effect of background warming trend on the spatial synchronization of DH events while accounting for inherent climate variability.

Following Hassan et al [26,27], the probability of experiencing a regional DH week is estimated using equation [3] below.

$$\hat{p}_i = \frac{n_i}{N} \quad [3]$$

Where $n_i$ is the number of DH weeks in region *i*, and N is the total number of weeks in consideration (here 2288 weeks for each region). Two regions (*i* and *j*) are under a synchronized DH if they experience a regional DH simultaneously on the given week. For each pair of regions (*i* and *j)*, the estimate of the probability of synchronized DH or synchronization probability ($\hat{p}_{i,j}$)

is the ratio of the number of synchronized DH weeks ($n_{ij}$) and the total number of weeks under consideration (N) as in equation [4].

$$\hat{p}_{i,j} = \frac{n_{ij}}{N} \quad [4]$$

If the regions are independent, the estimated synchronization probability is $\hat{p}_i \times \hat{p}_j$. Likelihood multiplication factor (LMF [19]) is used as a measure of the strength of synchronization between each pair of regions. The LMF is the ratio of the observed synchronization probability and synchronization probability under the complete independence assumption. For any pair of regions *i* and *j* LMF is computed as follows:

$$LMF_{ij} = \frac{\hat{p}_{i,j}}{\hat{p}_i \times \hat{p}_j} \quad [5]$$

The LMF ranges between 0 and infinity and a value of 1 indicates high likelihood of completely independent region pairs. However, if the observed synchronization is higher than what is expected under independence, LMF is significantly greater than 1 and opposite is the case for LMF less than 1.

To assess the statistical significance of LMF for each region pair, statistical significance test is performed based on the null hypothesis that the observed number of synchronized DHs can be reproduced by chance and does not require any physical relationship between the regions. To perform this, a bootstrapping procedure is adopted by generating 100,000 random resamples, each of sample size 1500, from binary regional DH arrays (DH week=1; no DH week=0) for each region separately (resample set 1) [without maintaining the time i.e., different weeks are compared for synchronization]. This eliminates the physical relationship between the regions and the temporal autocorrelation within the regions. Since the independent random resamples are of smaller sample

size (only 1500 weeks) compared to the actual observation (2288 weeks), bootstrapping method is used to produce an estimate of the observed DH weeks (sample size 1500) while preserving the physical relationship between the regions. This was accomplished by generating an additional 100,000 resamples of sample size 1500 by resampling all regions together based on datetime (resample set 2). The synchronized DH weeks for each pair of regions are computed for all resamples in both of the resample sets. The mean number of synchronized DH weeks (hereafter referred as "bootstrap mean", unless specified) for the Resample set 2 is representative of observed synchronized DH weeks. The LMF of a region pair is considered statistically significant at 1% significance level if the number of synchronized DH weeks in at least 99% of resamples from Resample set 1 (independent case) is lesser than the bootstrap mean for that pair. A bootstrapping-based field significance test is also performed using the procedure as in Rider et al [16].

To evaluate the robustness of the significant synchronization pairs, we also used one-tailed binomial test at 1% significance level to assess the statistical significance of synchronization (LMF values). The null hypothesis for binomial test is that the observed concordant probability is higher than what is expected under independence, i.e.,

$$H_o: \hat{p}_{i,j} \leq \hat{p}_i \times \hat{p}_j \quad [6]$$

$$H_a: \hat{p}_{i,j} > \hat{p}_i \times \hat{p}_j \quad [7]$$

To test for field significance, false discovery rate (FDR [75]) correction was applied to the p-values obtained from binomial tests.

## 6.5 Impact on primary productivity and crop yield

The impact of droughts, heatwaves, and compound drought-heatwave (DH) events on GPP [in g C $d^{-1}$] is quantified by comparing the GPP under extreme conditions to the GPP under normal

conditions. A normal condition is defined when there is no drought or heatwave. We included extreme precipitation events (SPI>1) and associated flooding as the normal conditions, because of their marginal and contrasting influence on GPP [76,77]. Excessive precipitation usually increases GPP whereas extreme precipitation followed by flooding reduces GPP [78]. Also, the change in GPP during extreme precipitation/flooding is significantly lower compared to dry and hot conditions [76]. For each week, the GPP loss is calculated separately for each grid cell and then averaged over the years to obtain the average GPP loss for that calendar week. Specifically, for any given week and a grid cell, the GPP change/loss due to a DH event is determined by subtracting the GPP during the DH week from the average GPP for that same week during normal years. For example, if the first week of June (1–7 June) at a grid cell is a DH event in the years 2010 and 2015, but is found to be normal in 13 other years (with the remaining 5 years experiencing either drought or heatwave), the GPP change for 2010 is calculated as the difference between the GPP observed in 2010 and the average GPP for that week over the 13 normal years (referred to as normal GPP). The same calculation is repeated for 2015, and the average GPP loss for June 1–7 is then the mean of the losses in 2010 and 2015. The average annual GPP loss during the DH events is then obtained by averaging the losses across all calendar weeks. Here we show the GPP losses as the percentage loss, which is computed for each week as the ratio of the GPP loss to the normal GPP (annual average normal GPP map is shown in Figures S3-S4). Mathematically this is expressed as:

$$GPP\ loss\ (\%) = \frac{GPP_{DH} - GPP_{normal}}{GPP_{normal}} \times 100 \qquad [8]$$

To estimate the global GPP loss attributed to synchronized DH events under a background warming world, we sum the GPP losses (in g C $d^{-1}$) across all grid cells affected by DHs for each week. This sum is then divided by the global normal GPP (sum of normal GPP across all grids

[Figure S9a]) for that week to estimate the global GPP loss in percentage. Specifically, global GPP loss for any week is computed as:

$$Global\ GPP\ loss\ (\%) = \frac{\sum_{i=1}^{n}(GPP_{DH} - GPP_{normal})_i}{\sum GPP_{normal}} \times 100 \quad [9]$$

Where $(GPP_{DH} - GPP_{normal})_i$ (in g C $d^{-1}$) is the GPP loss during DH week at grid "*i*" and *n* is the number of the grids under DH events during this week. $\sum GPP_{normal}$ (in g C $d^{-1}$) is the total GPP over the globe for that week. It is important to note that our approach does not completely disentangle the effects of gradual warming from those of concurrent DH events on GPP. Because both GPP and temperature show long-term increasing trends, part of the difference in GPP between DH and non-DH weeks may arise from the background warming itself, not only from threshold-crossing DH extremes. Thus, our estimates should be viewed as capturing the combined influence of background warming and DH extremes. This perspective highlights that the increasing frequency and persistence of DH events, when superimposed on rising temperatures, poses an escalating threat to ecosystem productivity. We employed linear regression and three different correlation methods (Pearson only shows linear relationship, whereas Spearman and Kendall tau also takes care of nonlinear relationships) to robustly identify the relationship between the synchronized DH area and the GPP anomalies.

We assessed the impact of DH events on crop yields by first identifying DH weeks occurring during the crop growing season at each grid cell. Since yield sensitivity is highest during flowering, pollination, and maturation, we also focused on the final 90 days of the season to represent this critical phase [45]. For each crop, we then computed the annual mean percentage of crop-growing area affected by DH events during both full growing season (Supplementary Material) and the critical phase (main text). Both affected areal extent and crop yields (expressed as anomalies

relative to their long-term mean) are linearly detrended before applying regression and correlation analyses to quantify their relationship.

To capture the role of spatial synchronization, we concentrated on the critical phases of the cropland. First, we identified dominant crop-growing regions for each calendar month (shown in Figure S17-S19), defined as regions with at least 2,500 km² of cropland in the critical phase. The threshold of 2,500 $km^2$ corresponds to the area of one grid cell at the equator, ensuring that only regions with substantial crop presence are considered. Second, a dominant crop growing region was classified as DH-affected if the maximum monthly affected crop area exceeded both 250 km² and 5% of its cropland extent. Third, we defined a regional DH month if at least one week within that month qualified as a regional DH week (see Section 6.3). These thresholds ensure that at least part of the cropping area is significantly impacted: the 250 km² (representing 10% of the areal threshold used to define regional cropping zones) sets the lower limit for the 5% criterion preventing very localized events from qualifying as regional DH events in crop areas, and in capturing cases where extremes occur at slightly different weeks within the same month.

By combining these three conditions, we produced a monthly binary dataset indicating whether a crop-growing region experienced a DH event (1) or not (0). From this dataset, we counted the number of DH affected regions per month for the three selected crops. Months with at least five affected regions for wheat and maize, or three for rice (reflecting fewer dominant rice regions), were defined as widespread synchronized events/months. Finally, we examined the association between the annual frequency of these synchronized months and annual yield anomalies using regression and correlation analyses. This approach allowed us to distinguish whether yield losses were primarily driven by large DH-affected areas within single regions or by simultaneous impacts across multiple crop-growing regions.

Furthermore, to enhance the robustness of our analysis, we fitted a generalized linear regression model between yield anomalies and synchronization, considering the total DH-area affected (Area affected) and the number of widespread synchronized events (Synchronized events) as predictors. We observed a strong interdependence between the total DH-area affected and the number of regions synchronously affected, which motivated the inclusion of an additional interaction term in the GLM. Since the predictors were not normally distributed, and to address potential multicollinearity, we standardized the predictand (i.e., yield) and predictor variables prior to model fitting to minimize bias [79]. The modified model equation is expressed as:

$$\text{Yield} = \alpha \times \text{Area affected} + \beta \times \text{Synchronized events} + \gamma \times (\text{Area affected} \times \text{Synchronized events}) + \epsilon \quad [10]$$

The coefficients α and β represent the main effects corresponding to the area affected and the synchronized events, whereas γ represents the interaction effect. ϵ is the random normally distributed error term. The main effect quantifies the change in the predictand (e.g., yield) due to a unit change in one predictor (e.g., area affected) while holding others constant. In contrast, the interaction effect describes how the influence of one predictor on the predictand varies with changes in the other predictor."

The finding of this study relies on a single observation-based dataset (CPC data), which may differ from other observational datasets or reanalysis products due to variations in spatial resolution and inherent uncertainties [80]. While we used sub-monthly weekly analysis to explore synchrony in DH events, synchronization could also occur on a daily scale, warranting further investigation to capture finer temporal patterns and impacts. The analysis assumes regional DH events as independent events in concordance estimation methods (e.g., LMF and binomial tests), which may oversimplify cases where multi-week regional events are common. We tested the robustness of our

results to alternative threshold definitions for both drought-heatwave events and their regional aggregation. For drought, SPI thresholds were varied between –0.5 and –1.5, and for heatwaves, Tmax thresholds ranged from the 85th to the 95th percentile. Across all the combinations, the elevated risk of spatially synchronized DH events after 2000 remained evident (Figures S20-S21). Though the frequency of events reduced with more stringent thresholds, the overall patterns and conclusions remained robust. Likewise, for defining regional DH events, we varied the overlap requirement for concurrent DH area from 3% to 10%, while maintaining the 15% thresholds for individual drought and heatwave coverage (Figures S22-S23). Again, higher thresholds lowered the absolute magnitude of risk but did not alter the qualitative outcomes. These sensitivity tests confirm that our findings are not artifacts of threshold selection but instead reflect a robust and systematic increase in synchronized DH risk under a warming climate."

## 7 Data Availability

This study uses National Oceanic and Atmospheric Administration (NOAA) Climate Prediction Centre's (CPC) Global Unified Gauge-Based Analysis of Daily Precipitation and Temperature dataset, which are freely available at https://psl.noaa.gov/data/gridded/data.cpc.globalprecip.html and https://psl.noaa.gov/data/gridded/data.cpc.globaltemp.html.

The monthly crop-physical area data for the three selected staple crops (Rice, Maize, and Wheat) was obtained from the "GAEZ+_2015 Monthly Cropland Data", which is retrieved https://mygeohub.org/publications/60/1. Daily estimates of global gross primary productivity (GPP) were obtained from the FluxSat v2.0 dataset, available at https://daac.ornl.gov/VEGETATION/guides/FluxSat_GPP_FPAR.html. The crop yield and population estimates are retrieved from https://www.fao.org/faostat/en/#data/QCL.

## 8 Code Availability

The codes used in this study are developed in Python 3.11, and are made available via GitHub: http://github.com/waqar7006/Synchronized_compound_dry_hot_events.

## 9 Acknowledgements

Md Saquib Saharwardi, Harikishan Gandham, Hari Prasad Dasari reports financial support by the Climate Change Center, an initiative of the National Center for Meteorology (NCM), Kingdom of Saudi Arabia (Ref No: RGC/03/4829-01-01). We extend our sincere gratitude to our colleagues at the National Institute of Technology Srinagar and Climate Change Center, King Abdullah University of Science and Technology for their support, insightful discussions, and constructive feedback throughout this study. We would like to thank the National Oceanic and Atmospheric Administration (NOAA), the Food and Agriculture Organization (FAO), and the National

Aeronautics and Space Administration's MODIS project, for archiving and enabling public access to their data.

## 10 Author Contributions

W.U.H conceived and designed the study, analyzed the data, and wrote the paper. M.A.N, M.S.S, H. G, H.P.D, C. A, D. Y helped in design and co-wrote the manuscript. I.H, and Y.A supervised and helped in editing and writing final draft. All authors participated in the interpretation of results.

## 11 Declaration of interests

The authors declare that they have no known competing financial interests or personal relationships that could have appeared to influence the work reported in this paper.

## 12 References


1. García-Herrera, R., Díaz, J., Trigo, R. M., Luterbacher, J. & Fischer, E. M. A Review of the European Summer Heat Wave of 2003. *Critical Reviews in Environmental Science and Technology* **40**, 267–306 (2010).

2. Wegren, S. K. Food Security and Russia's 2010 Drought. *Eurasian Geography and Economics* **52**, 140–156 (2011).

3. Christian, J. I., Basara, J. B., Hunt, E. D., Otkin, J. A. & Xiao, X. Flash drought development and cascading impacts associated with the 2010 Russian heatwave. *Environmental Research Letters* **15**, 094078 (2020).

4. Beillouin, D., Schauberger, B., Bastos, A., Ciais, P. & Makowski, D. Impact of extreme weather conditions on European crop production in 2018. *Phil. Trans. R. Soc. B* **375**, 20190510 (2020).

5. Mishra, A., Ray, L. K. & Reddy, V. M. Effects of compound hydro-meteorological extremes on rice yield in different cultivation practices in India. *Theor Appl Climatol* **155**, 4507–4520 (2024).

6. Zscheischler, J. *et al.* A typology of compound weather and climate events. *Nature reviews earth & environment* **1**, 333–347 (2020).

7. Lesk, C. *et al.* Compound heat and moisture extreme impacts on global crop yields under climate change. *Nature Reviews Earth & Environment* **3**, 872–889 (2022).

8. Fahad, S. *et al.* Crop production under drought and heat stress: plant responses and management options. *Frontiers in plant science* **8**, 1147 (2017).

9. Rezaei, E. E. *et al.* Climate change impacts on crop yields. *Nature Reviews Earth & Environment* **4**, 831–846 (2023).

10. Purushothaman, R. *et al.* Association of mid-reproductive stage canopy temperature depression with the molecular markers and grain yields of chickpea (Cicer arietinum L.) germplasm under terminal drought. *Field Crops Research* **174**, 1–11 (2015).

11. Bador, M. *et al.* Future summer mega-heatwave and record-breaking temperatures in a warmer France climate. *Environmental Research Letters* **12**, 074025 (2017).

12. Abdelhakim, L. O. A., Zhou, R. & Ottosen, C.-O. Physiological responses of plants to combined drought and heat under elevated CO2. *Agronomy* **12**, 2526 (2022).

13. Jarrett, U., Miller, S. & Mohtadi, H. Dry spells and global crop production: A multi-stressor and multi-timescale analysis. *Ecological Economics* **203**, 107627 (2023).

14. Hunt, E. *et al.* Agricultural and food security impacts from the 2010 Russia flash drought. *Weather and Climate Extremes* **34**, 100383 (2021).

15. Mishra, V., Thirumalai, K., Singh, D. & Aadhar, S. Future exacerbation of hot and dry summer monsoon extremes in India. *Npj Climate and Atmospheric Science* **3**, 10 (2020).

16. Ridder, N. N. *et al.* Global hotspots for the occurrence of compound events. *Nature communications* **11**, 5956 (2020).

17. Koster, R. D. *et al.* Regions of Strong Coupling Between Soil Moisture and Precipitation. *Science* **305**, 1138–1140 (2004).

18. Saharwardi, M. S. *et al.* Rising occurrence of compound droughts and heatwaves in the Arabian Peninsula linked to large-scale atmospheric circulations. *Science of The Total Environment* **978**, 179433 (2025).

19. Zscheischler, J. & Seneviratne, S. I. Dependence of drivers affects risks associated with compound events. *Sci. Adv.* **3**, e1700263 (2017).

20. Alizadeh, M. R. *et al.* A century of observations reveals increasing likelihood of continental-scale compound dry-hot extremes. *Sci. Adv.* **6**, eaaz4571 (2020).

21. Herrera-Estrada, J. E. *et al.* Reduced Moisture Transport Linked to Drought Propagation Across North America. *Geophysical Research Letters* **46**, 5243–5253 (2019).

22. Zhuang, Y. *et al.* Anthropogenic warming has ushered in an era of temperature-dominated droughts in the western United States. *Sci. Adv.* **10**, eadn9389 (2024).

23. He, Y., Hu, X., Xu, W., Fang, J. & Shi, P. Increased probability and severity of compound dry and hot growing seasons over world′s major croplands. *Science of the Total Environment* **824**, 153885 (2022).

24. Mazdiyasni, O. & AghaKouchak, A. Substantial increase in concurrent droughts and heatwaves in the United States. *Proc. Natl. Acad. Sci. U.S.A.* **112**, 11484–11489 (2015).

25. Mukherjee, S. & Mishra, A. K. Increase in Compound Drought and Heatwaves in a Warming World. *Geophysical Research Letters* **48**, e2020GL090617 (2021).

26. Hassan, W. ul, Nayak, M. A. & Azam, M. F. Intensifying spatially compound heatwaves: Global implications to crop production and human population. *Science of The Total Environment* **932**, 172914 (2024).

27. Hassan, W. U. & Nayak, M. A. Global teleconnections in droughts caused by oceanic and atmospheric circulation patterns. *Environmental Research Letters* **16**, 014007 (2020).

28. Singh, J., Ashfaq, M., Skinner, C. B., Anderson, W. B. & Singh, D. Amplified risk of spatially compounding droughts during co-occurrences of modes of natural ocean variability. *npj Climate and Atmospheric Science* **4**, 7 (2021).

29. Boers, N. *et al.* Complex networks reveal global pattern of extreme-rainfall teleconnections. *Nature* **566**, 373–377 (2019).

30. Kornhuber, K. *et al.* Amplified Rossby waves enhance risk of concurrent heatwaves in major breadbasket regions. *Nature Climate Change* **10**, 48–53 (2020).

31. Rogers, C. D., Kornhuber, K., Perkins-Kirkpatrick, S. E., Loikith, P. C. & Singh, D. Sixfold increase in historical Northern Hemisphere concurrent large heatwaves driven by warming and changing atmospheric circulations. *Journal of Climate* **35**, 1063–1078 (2022).

32. Branstator, G. Circumglobal teleconnections, the jet stream waveguide, and the North Atlantic Oscillation. *Journal of Climate* **15**, 1893–1910 (2002).

33. Alexander, M. A. *et al.* The atmospheric bridge: The influence of ENSO teleconnections on air–sea interaction over the global oceans. *Journal of climate* **15**, 2205–2231 (2002).

34. Bevacqua, E., Zappa, G., Lehner, F. & Zscheischler, J. Precipitation trends determine future occurrences of compound hot–dry events. *Nature Climate Change* **12**, 350–355 (2022).

35. Zhou, S., Yu, B. & Zhang, Y. Global concurrent climate extremes exacerbated by anthropogenic climate change. *Sci. Adv.* **9**, eabo1638 (2023).

36. Stendel, M., Francis, J., White, R., Williams, P. D. & Woollings, T. The jet stream and climate change. in *Climate change* 327–357 (Elsevier, 2021).

37. Corti, S., Molteni, F. & Palmer, T. N. Signature of recent climate change in frequencies of natural atmospheric circulation regimes. *Nature* **398**, 799–802 (1999).

38. Kornhuber, K. *et al.* Risks of synchronized low yields are underestimated in climate and crop model projections. *Nature Communications* **14**, 3528 (2023).

39. Gaupp, F., Hall, J., Hochrainer-Stigler, S. & Dadson, S. Changing risks of simultaneous global breadbasket failure. *Nature Climate Change* **10**, 54–57 (2020).

40. Mehrabi, Z. & Ramankutty, N. Synchronized failure of global crop production. *Nature ecology & evolution* **3**, 780–786 (2019).

41. Bellemare, M. F. Rising Food Prices, Food Price Volatility, and Social Unrest. *American J Agri Economics* **97**, 1–21 (2015).

42. Zscheischler, J. *et al.* A few extreme events dominate global interannual variability in gross primary production. *Environmental Research Letters* **9**, 035001 (2014).

43. Schumacher, D. L. *et al.* Amplification of mega-heatwaves through heat torrents fuelled by upwind drought. *Nature Geoscience* **12**, 712–717 (2019).

44. Miralles, D. G., Gentine, P., Seneviratne, S. I. & Teuling, A. J. Land–atmospheric feedbacks during droughts and heatwaves: state of the science and current challenges. *Annals of the New York Academy of Sciences* **1436**, 19–35 (2019).

45. Heino, M. *et al.* Increased probability of hot and dry weather extremes during the growing season threatens global crop yields. *Scientific reports* **13**, 3583 (2023).

46. He, Y., Fang, J., Xu, W. & Shi, P. Substantial increase of compound droughts and heatwaves in wheat growing seasons worldwide. *Intl Journal of Climatology* **42**, 5038–5054 (2022).

47. Zhu, P., Abramoff, R., Makowski, D. & Ciais, P. Uncovering the Past and Future Climate Drivers of Wheat Yield Shocks in Europe With Machine Learning. *Earth's Future* **9**, e2020EF001815 (2021).

48. Siebert, S. *et al.* The digital global map of irrigation areas–development and validation of map version 4. in *Conference on International Agricultural Research for Development (Tropentag)* (2006).

49. Grogan, D., Frolking, S., Wisser, D., Prusevich, A. & Glidden, S. Global gridded crop harvested area, production, yield, and monthly physical area data circa 2015. *Scientific data* **9**, 15 (2022).

50. Liliane, T. N. & Charles, M. S. Factors affecting yield of crops. *Agronomy-climate change & food security* 9 (2020).

51. Yao, Y., Liu, Y., Zhou, S., Song, J. & Fu, B. Soil moisture determines the recovery time of ecosystems from drought. *Global Change Biology* **29**, 3562–3574 (2023).

52. Jiao, T., Williams, C. A., De Kauwe, M. G., Schwalm, C. R. & Medlyn, B. E. Patterns of post-drought recovery are strongly influenced by drought duration, frequency, post-drought wetness, and bioclimatic setting. *Global Change Biology* **27**, 4630–4643 (2021).

53. Sheffield, J., Wood, E. F. & Roderick, M. L. Little change in global drought over the past 60 years. *Nature* **491**, 435–438 (2012).

54. Zhang, P. *et al.* Abrupt shift to hotter and drier climate over inner East Asia beyond the tipping point. *Science* **370**, 1095–1099 (2020).

55. Huang, J. *et al.* Recently amplified arctic warming has contributed to a continual global warming trend. *Nature climate change* **7**, 875–879 (2017).

56. Dang, C. *et al.* Climate warming-induced phenology changes dominate vegetation productivity in Northern Hemisphere ecosystems. *Ecological Indicators* **151**, 110326 (2023).

57. Zhang, Y., Xu, M., Chen, H. & Adams, J. Global pattern of NPP to GPP ratio derived from MODIS data: effects of ecosystem type, geographical location and climate. *Global Ecology and Biogeography* **18**, 280–290 (2009).

58. CPC, C. Global Temperature and Unified Precipitation data provided by the NOAA PSL. PSL, Boulder, Colorado, USA (2020). (2020).

59. Reichle, R. H. *et al.* Assessment of MERRA-2 land surface hydrology estimates. *Journal of Climate* **30**, 2937–2960 (2017).

60. Hersbach, H. *et al.* The ERA5 global reanalysis. *Quart J Royal Meteoro Soc* **146**, 1999–2049 (2020).

61. Beck, H. E. *et al.* Global-scale evaluation of 22 precipitation datasets using gauge observations and hydrological modeling. *Hydrology and Earth System Sciences* **21**, 6201–6217 (2017).

62. Frolking, S. *et al.* GAEZ+ _2015 global gridded crop harvest area, crop production, and crop yield-Metadata. *Harvard Dataverse* https://data.apps.fao.org/map/catalog/srv/api/records/7f8f21a1-452d-4ab5-a83a-f2cbccd15027/attachments/GAEZ%202015%20metadata.pdf (2020).

63. Grogan, D., Prusevich, A., Frolking, S., Wisser, D. & Glidden, S. GAEZ _2015 Monthly Cropland Data: Global gridded monthly crop physical area for 26 irrigated and rainfed crops. https://doi.org/10.13019/J2BH-VB41 (2021) doi:10.13019/J2BH-VB41.

64. Joiner, J. & Yoshida, Y. Satellite-based reflectances capture large fraction of variability in global gross primary production (GPP) at weekly time scales. *Agricultural and Forest Meteorology* **291**, 108092 (2020).

65. FAOSTAT. https://www.fao.org/faostat/en/#data/QCL.

66. McKee, T. B., Doesken, N. J. & Kleist, J. The relationship of drought frequency and duration to time scales. in *Proceedings of the 8th Conference on Applied Climatology* vol. 17 179–183 (Boston, 1993).

67. Vicente-Serrano, S. M., Beguería, S. & López-Moreno, J. I. A multiscalar drought index sensitive to global warming: the standardized precipitation evapotranspiration index. *Journal of climate* **23**, 1696–1718 (2010).

68. Hassan, W. ul, Nayak, M. A. & Lyngwa, R. V. Recent changes in heatwaves and maximum temperatures over a complex terrain in the Himalayas. *Science of the Total Environment* **794**, 148706 (2021).

69. Hassan, W. ul *et al.* Unveiling the devastating effect of the spring 2022 mega-heatwave on the South Asian snowpack. *Communications Earth & Environment* **5**, 707 (2024).

70. Forster, P., Storelvmo, T. & Alterskjæ, K. IPCC sixth assessment report (AR6) working group 1: the physical science basis, chap. 7. (2021).

71. Iturbide, M. *et al.* An update of IPCC climate reference regions for subcontinental analysis of climate model data: definition and aggregated datasets. *Earth System Science Data* **12**, 2959–2970 (2020).

72. Enfield, D. B., Mestas-Nuñez, A. M. & Trimble, P. J. The Atlantic Multidecadal Oscillation and its relation to rainfall and river flows in the continental U.S. *Geophysical Research Letters* **28**, 2077–2080 (2001).

73. Lee, S. *et al.* Rapidly Changing East Asian Marine Heatwaves Under a Warming Climate. *JGR Oceans* **128**, e2023JC019761 (2023).

74. Chan, D. & Wu, Q. Attributing observed SST trends and subcontinental land warming to anthropogenic forcing during 1979–2005. *Journal of Climate* **28**, 3152–3170 (2015).

75. Benjamini, Y. & Yekutieli, D. The control of the false discovery rate in multiple testing under dependency. *Annals of statistics* 1165–1188 (2001).

76. Zscheischler, J. *et al.* Impact of large-scale climate extremes on biospheric carbon fluxes: An intercomparison based on MsTMIP data. *Global Biogeochemical Cycles* **28**, 585–600 (2014).

77. Balashov, N. V. *et al.* Flood Impacts on Net Ecosystem Exchange in the Midwestern and Southern United States in 2019. *JGR Atmospheres* **128**, e2022JD037697 (2023).

78. Piao, S. *et al.* The impacts of climate extremes on the terrestrial carbon cycle: A review. *Sci. China Earth Sci.* **62**, 1551–1563 (2019).

79. Marquardt, D. W. Comment: You Should Standardize the Predictor Variables in Your Regression Models. *Journal of the American Statistical Association* **75**, 87–91 (1980).

80. Jiang, L. *et al.* Identification and characterization of global compound heat wave: comparison from four datasets of ERA5, Berkeley Earth, CHIRTS and CPC. *Clim Dyn* **62**, 631–648 (2024).

13 Figures

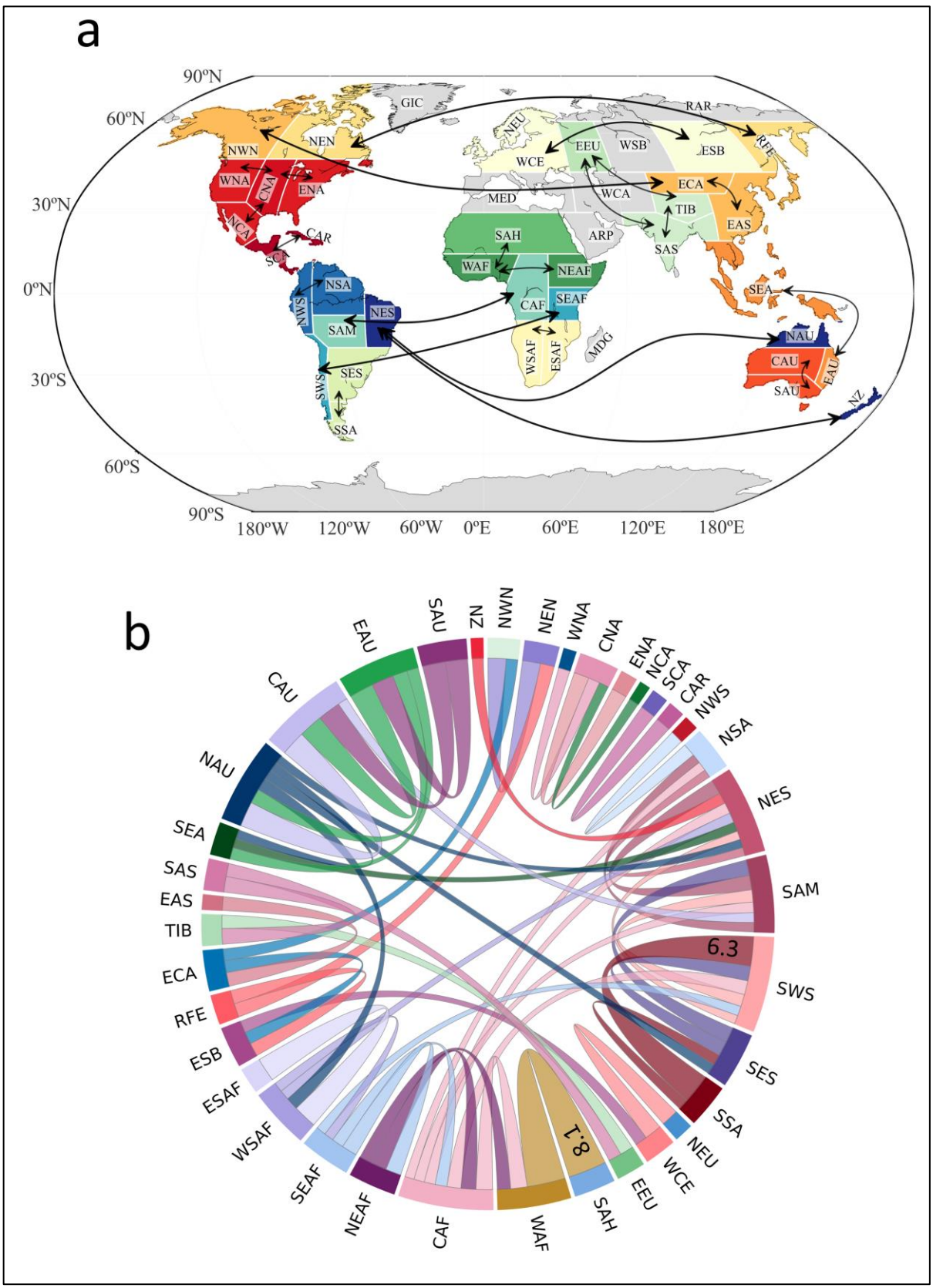
a
90°N
60°N
30°N
0°N
30°S
60°S
90°S
180°W
120°W
60°W
0°E
60°E
120°E
180°E
GIC
NWN
NEN
WNA
CNA
ENA
NCA
SCA
CAR
NSA
NWS
NES
SAM
SWS
SES
SSA
RAR
NEU
WCE
EEU
WSB
ESB
RFE
MED
WCA
ECA
TIB
EAS
SAS
ARP
SAH
WAF
NEAF
CAF
SEAF
WSAF
ESAF
MDG
SEA
NAU
CAU
EAU
SAU
NZ
b
SAU
NZ
NWN
NEN
WNA
CNA
ENA
NCA
SCA
CAR
NWS
NSA
NES
SAM
SWS
SES
SSA
NEU
WCE
EEU
SAH
WAF
CAF
NEAF
SEAF
WSAF
ESAF
RFE
ESB
ECA
TIB
EAS
SAS
SEA
NAU
CAU
EAU
6.3
8.1

***Figure 1. Potential region pairs with synchronized DHs.*** *(a) Significantly robust (statistically significant at 1% in both binomial test and bootstrapping [see Figure S1 for separate plots]) synchronized region pairs that experience regional DHs together, i.e., region pairs that have a higher probability of synchronous DHs compared to what is expected by chance. The regions on the map with the same color and connected by the arrows show robust synchronization. While regions in grey color do not show concordance with any other region. Only one to two connections are shown for each region, and long-distance connections are given priority to clarify the spatial relationship (b) Chord plot showing all significant synchronization of each region. The widths of the chords/links represent the LMF values of the synchronization (annotated for two chords as a scale). Interactive plots (link) are provided for retrieving the LMF strength of all pairs. The link contains a folder and files. Once downloaded, the user can open the interactive plot by just opening the file. Since the distance between the regions is not given in (a), we show at-least one synchronization for each region (priority given to long-distance connections) on a map.*

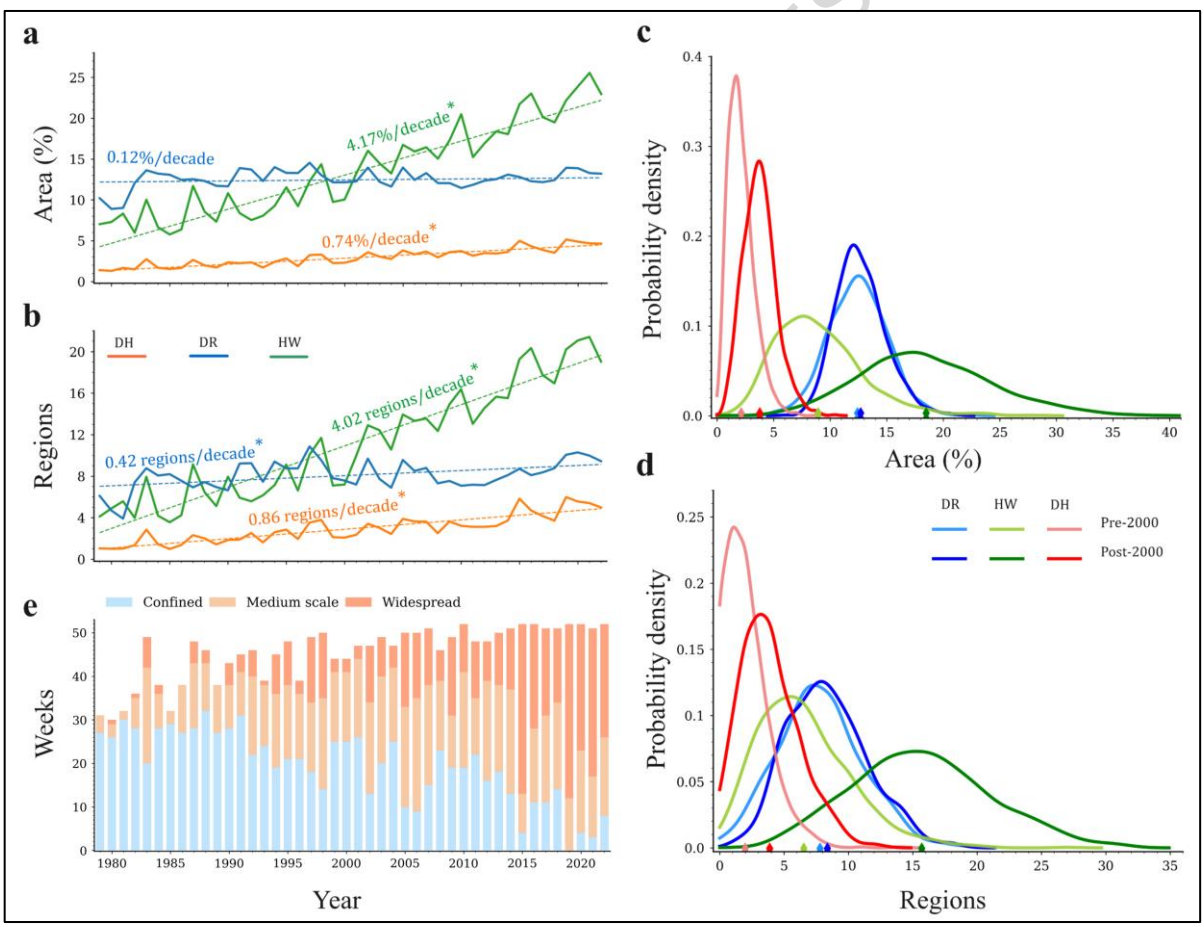


***Figure 2. Temporal changes in spatial synchrony in DH events.*** *(a) the proportion (in percent of total land) of global terrestrial land and (b) the number of IPCC reference regions, excluding Antarctica, under synchronous dry (indicated in blue), hot (in green), and DH events (in orange) spanning the years 1979 to 2022. (c) and (d) the probability distribution of the global areal extent and number of IPCC regions under dry (blue shades), hot (green shades), and DH (red shades)*

*during the pre-2000 (light shade) and post-2000 (dark shade). (e) shows the temporal variability of the confined (1 and 2 regions; blue color), medium scale (3 and 4 regions; orange color), and widespread (5 or more regions; red color) DH events. The text numbers in (a) and (b) represent the trend values and the asterisk represents the statistical significance at 5%.*

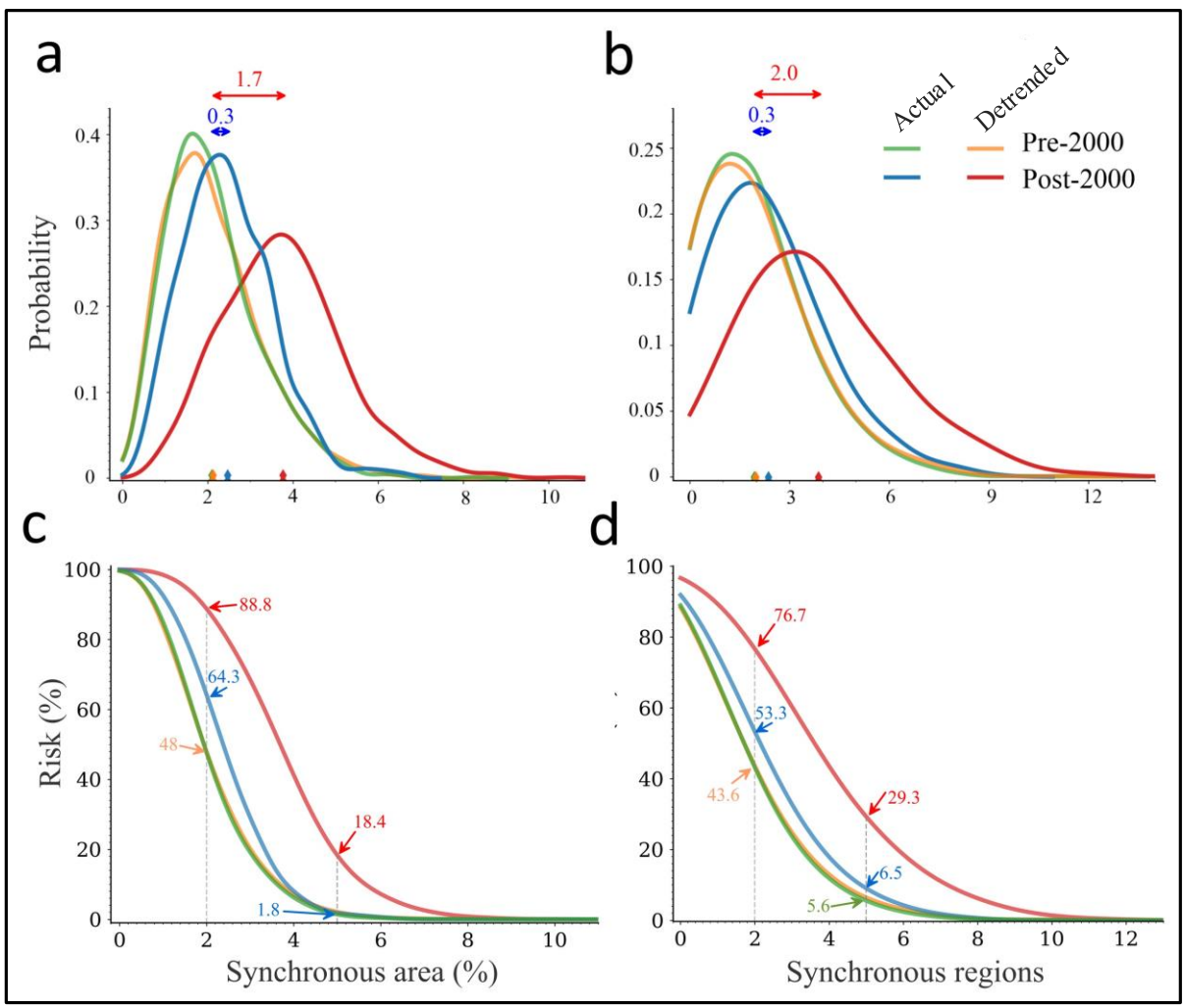


***Figure 3. Change in risk of synchronization in DHs due to warming trend.*** *(a) and (b) are the probability density of global land area (in percentage of total land, excluding Antarctica) and number of IPCC regions affected by DHs synchronously during pre-2000 (green and orange) and post-2000 (blue and red) based on* ***actual scenario*** *(actual temperature [orange and red color]) and* ***detrended scenario*** *(detrended temperature [green and blue color]). The diamonds on the x-axis represent the means of the distributions, and the numbers on double-headed arrows represent the change in the mean of pre-2000 and post-2000 distribution for detrended (blue arrow and numbers) and actual (red arrow and numbers) analysis. Change in pre-2000 and post-2000 risk (change in exceedance probability) of synchronization of DHs based on synchrony in (c) global extent affected and (d) number of IPCC region. The color coding is the same as in (a and b). The numbers represent the percentage risk (exceedance probability ×100). The change in risk of widespread events is a difference of post- and pre-2000 risk corresponding to 5 regions. However, the case of confined events is different, where non-exceedance risks are first calculated, which are then subtracted to get change risk (details in Methods).*

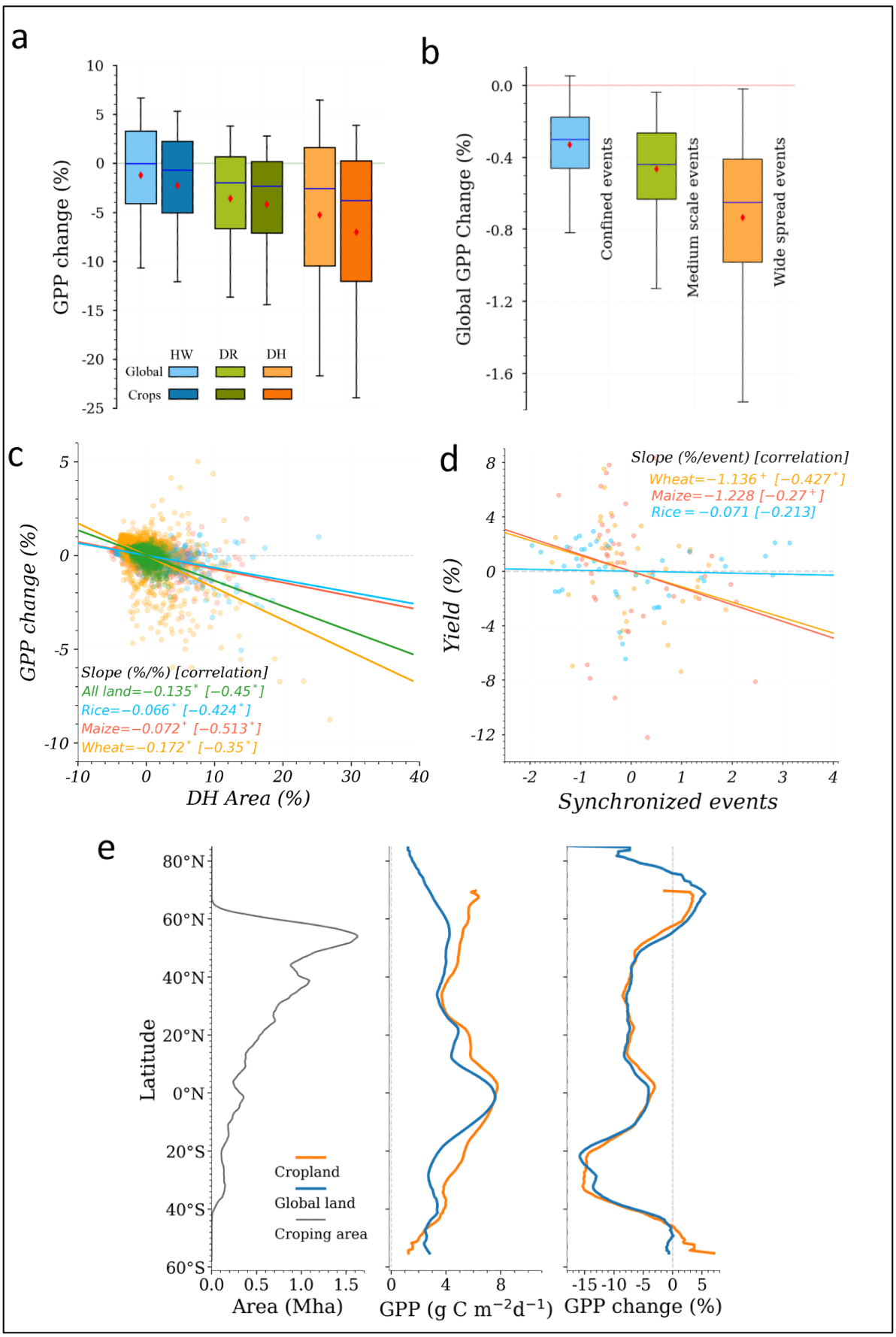
a
GPP change (%)
HW
DR
DH
Global
Crops
b
Global GPP Change (%)
Confined events
Medium scale events
Wide spread events
c
GPP change (%)
Slope (%/%) [correlation]
All land=−0.135* [−0.45*]
Rice=−0.066* [−0.424*]
Maize=−0.072* [−0.513*]
Wheat=−0.172* [−0.35*]
DH Area (%)
d
Slope (%/event) [correlation]
Wheat=−1.136+ [−0.427*]
Maize=−1.228 [−0.27+]
Rice = −0.071 [−0.213]
Yield (%)
Synchronized events
e
Latitude
80°N
60°N
40°N
20°N
0°N
20°S
40°S
60°S
Cropland
Global land
Croping area
Area (Mha)
GPP (g C m−2d−1)
GPP change (%)

***Figure 4. Impact of synchronized DHs on Global primary productivity and yield***. *(a) Distribution of gross primary productivity loss during the dry, hot, and DH events in cropland and global land (b) Percentage change in the total global landmass GPP with the number of regions synchronously affected by DHs. The confined, medium-scale, and widespread events are defined when one or two regions, three or four regions, and five or more regions are synchronously affected by DHs. The red line corresponds to no change in GPP (i.e., normal GPP as in Figure S7a). (c) Variation of detrended percentage change in the GPP with the detrended percentage of the land area under the DHs in all three croplands and global landmass during the period 1979–2022. The dashed grey line corresponds to a zero percent change in GPP. (d) The variation of detrended percentage crop yield (percentage as mean yield during 1979–2021) with detrended number of widespread synchronized DH events in croplands for three selected crops. (e) Latitudinal variation (estimated using a 10-degree latitudinal band centered on the latitude) of the annual average cropland area (left panel), normal GPP conditions (middle panel), and GPP loss during DH events (right panel). The dashed grey line corresponds to no change in yield. The linear regression slope and Spearman correlation are mentioned in the colored text with the asterisk representing that the values are statistically significant at 5% significance level. Pearson correlation and Kendall tau are shown in Table S4. The red dots in (a) and (b) represent the mean. The whiskers correspond to 10 and 90 percentiles in (a) and 2.5 and 97.5 percentiles in (b).*

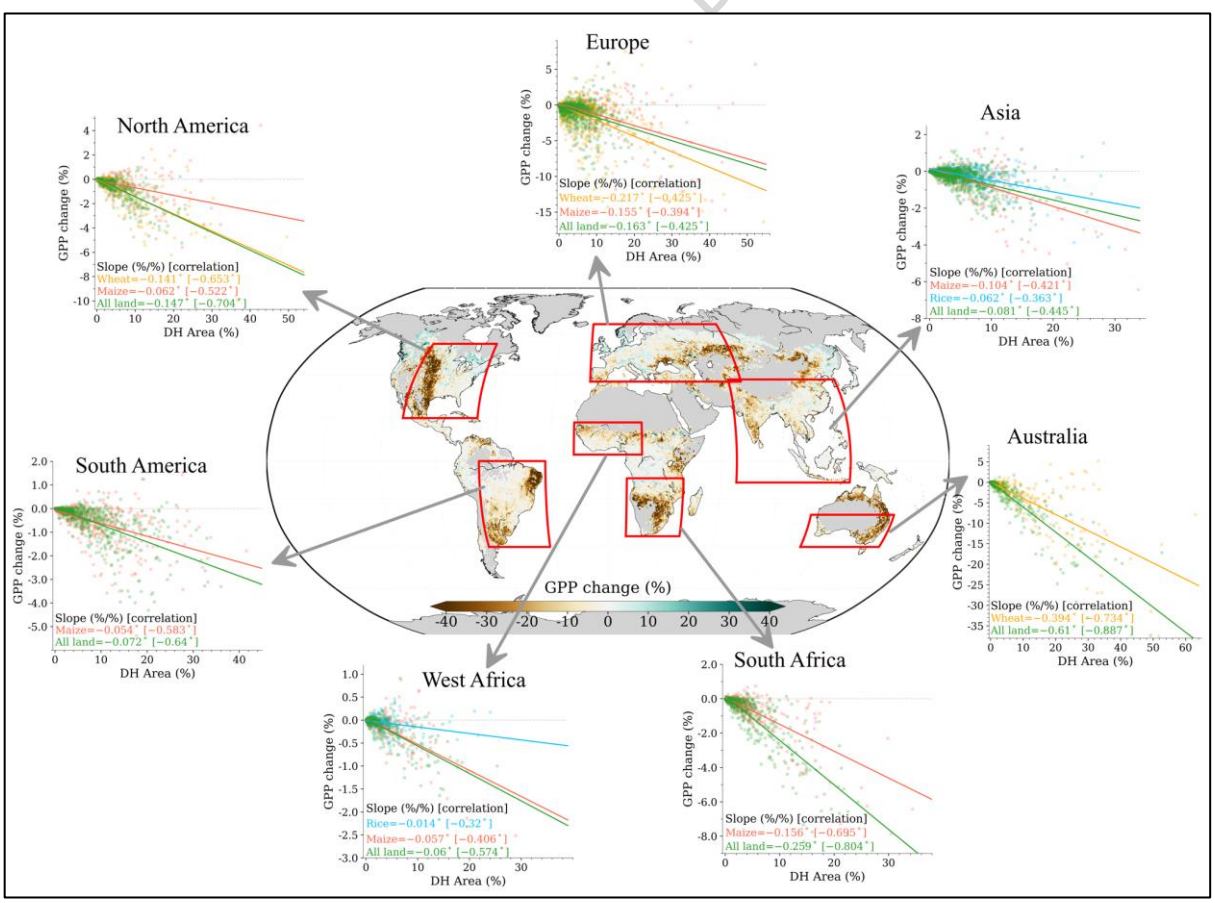


***Figure 5. Impact of synchronized DHs on primary productivity and agriculture in the breadbasket regions***. *The map shows the spatial distribution primary productivity change during DH events in cropland grid cells. The inset plots are same as Figure 4c but for regional primary*

*productivity change during the major crop growing season. Some regions have two major crops for example rice and maize in Asia. The linear regression slope and Spearman correlation are mentioned in the colored text with the asterisk representing that the values are statistically significant at 5% significance level. Pearson correlation and Kendall tau are shown in Table S5. The dashed grey line corresponds to a zero percent change in GPP.*

**Editorial summary:**
Widespread spatial synchrony of dry-hot events has been more frequent over the past four decades, increasing nearly ten folds, and reduces global ecosystem productivity and crop yields, based on survey, reanalysis, and remote sensing-based datasets.

**Peer review information:**

*Communications Earth and Environment* thanks Lina Zhang and the other, anonymous, reviewer(s) for their contribution to the peer review of this work. Primary Handling Editors: Fiona Tang, Aliénor Lavergne, and Mengjie Wang. [A peer review file is available.]